

Correlated Disorder Substrate-Integrated Nanodisk Scatterers for Light Extraction in Organic Light Emitting Diodes

Peter M. Piechulla,* Yidenekachew J. Donie, Ralf B. Wehrspohn, Uli Lemmer, Guillaume Gomard, and Alexander N. Sprafke*

A major loss mechanism in organic light emitting diodes (OLEDs) is the coupling of the emitter molecule light field to waveguide modes in the OLED thin film stack. In this work, a disordered 2D array of TiO₂ nanodisk scatterers is integrated into the OLED substrate to enable efficient light extraction from these waveguide modes. Fabrication of the nanodisks is based on a bottom-up, colloidal lithography technique and subsequent pattern transfer into high refractive index TiO₂ via reactive ion etching. The substrates are completed by spin-coating a polymer planarization layer before applying the OLED thin film stack. This ensures reproducible optoelectronic properties of the OLED through leaving the electrically active layers planar. Simultaneously, the nanodisks in close vicinity to the thin film stack ensure efficient out-of-plane scattering of waveguide modes. In a monochromatic OLED (center wavelength $\lambda_0 = 520$ nm), a 44.2%_{rel} increase in external quantum efficiency is achieved in comparison to a device without scattering structure. An in-depth numerical analysis reveals that this significant enhancement is only partly due to the out-coupling of waveguide modes. Additional enhancement is suspected to result from out-coupling of substrate modes through scattering by the nanodisks. Further improvements to the scattering structure are numerically evaluated.

the same time, OLEDs are yet to be commercialized on a similarly large scale in lighting applications, where such devices may soon enable new design conventions, for example, lighting planes replacing conventional point sources. Regardless of the application, the efficiency of OLED devices is of central importance, may it be for longer battery life in a mobile device, or for lower energy consumption for larger scale lighting applications.

In any optoelectronic device, refractive index discontinuities typically reduce light coupling between the device and its surrounding. In the case of OLEDs, this results in light trapping effects which, in combination with absorbing electrode materials, effectively attenuate the external quantum efficiency (EQE).^[1] More specifically, a first major optical loss path is total internal reflection within the substrate, which can be overcome by structuring the air-substrate interface,

that is, applying an external scattering structure. Suggested solutions to this issue range from simply sandblasting the substrates,^[2] to standard microlens arrays,^[3] to sophisticated bio-mimetic, hierarchical patterning,^[4] all of which have in

1. Introduction


Organic light emitting diodes (OLEDs) are widely used in display applications for mobile and stationary electronic devices. At

P. M. Piechulla, R. B. Wehrspohn, A. N. Sprafke
Institute of Physics
Martin Luther University Halle-Wittenberg
06120 Halle, Germany
E-mail: peter.piechulla@physik.uni-halle.de;
alexander.sprafke@physik.uni-halle.de
R. B. Wehrspohn
Distinguished Adjunct Professor
Korean Institute of Energy Technologie KENTECH
200 Hyeoksins-ro, Naju 58330, South Korea

Y. J. Donie, U. Lemmer, G. Gomard
Light Technology Institute
Karlsruhe Institute of Technology
Engesserstrasse 13, 76131 Karlsruhe, Germany

Y. J. Donie
Department of Chemical Engineering and Material Science
College of Science and Engineering
University of Minnesota
421 Washington Ave. SE, Minneapolis, MN 55455-0132, USA

U. Lemmer, G. Gomard
Institute of Microstructure Technology
Karlsruhe Institute of Technology
Hermann-von-Helmholtz-Platz 1, 76344 Eggenstein-Leopoldshafen, Germany
G. Gomard
Carl Zeiss AG
Zeiss Innovation Hub
Hermann-von-Helmholtz-Platz 6, 76344 Eggenstein-Leopoldshafen, Germany

 The ORCID identification number(s) for the author(s) of this article can be found under <https://doi.org/10.1002/adom.202202557>.

© 2023 The Authors. Advanced Optical Materials published by Wiley-VCH GmbH. This is an open access article under the terms of the Creative Commons Attribution-NonCommercial-NoDerivs License, which permits use and distribution in any medium, provided the original work is properly cited, the use is non-commercial and no modifications or adaptations are made.

DOI: 10.1002/adom.202202557

common that the electrically active layers remain virtually unaffected.^[5,6]

A second major loss path is via modes within high refractive index transparent contact and organic layers, and surface plasmon polaritons (SPP) at the metallic rear contact of the device.^[7,8] Both may be summarized as waveguide modes and can make up to $\approx 50\%$ of the emitted power by the emitter molecules.^[1] In general terms, there are at least three non-exclusive approaches to address this issue. The first is to tune the orientation of the emitter molecules, that is, to horizontally aligned dipole moments,^[9–11] such that coupling to waveguide modes is reduced. The second approach is to reduce the number of modes by reducing the thicknesses of the high refractive index layers, as has recently been demonstrated by replacing the transparent contact layer with a much thinner metallic layer.^[12] The third approach is to incorporate a light management structure within or near the thin film stack (an internal scattering structure) to enable coupling of waveguide modes to substrate propagating modes from which they can be extracted to radiating modes. An obvious design approach for internal scattering structures is to fabricate the organic and contact layers on the basis of nanotextured substrates^[13] which are often implemented using a form of self-assembly process.^[14–17] Here, the spectral density of the interface profile can be tuned to match the wavevectors of the waveguide modes,^[18,19] depending on the emission color of the respective OLED device. This approach leads to a notable increase in EQE; however, the corrugated substrate also implies thickness inhomogeneities of the organic layers and often leads to degradation of the electrical properties. Another design approach for internal scattering structures is volumetric scattering layers of several micrometer thickness, which are based on light scatterers dispersed in a host matrix with a sufficient refractive index contrast between the two, and ideally achieving refractive index matching with the OLED stack to foster spatial overlap of the confined modes with this outcoupling layer.^[20–22] While these layers scatter strongly and indeed improve light extraction, they also tend to reduce the overall transmittance compared to a planar glass interface due to multiple scattering and hence enhanced back-scattering.^[22]

An alternative is thin, compact layers with integrated scattering structures,^[23,24] such as 2D arrays of scatterers.^[25–27] Here, scattering is achieved by a spatial modulation of the refractive index rather than by nanotextured interfaces. Typically, the scatterers are first deposited or fabricated on top of a planar interface and subsequently planarized by a spin-coated polymer layer. Donie et al. recently demonstrated improved EQEs by $\approx 22\%_{\text{rel}}$ by such an internal light scattering layer of only 250 nm thickness and embedded polydisperse TiO₂ nanopillars with broadband, angular-stable light scattering properties.^[27]

In the present work, we fabricate arrays of nanodisk scatterers using a bottom-up, scalable method based on colloidal self-assembly and subsequent pattern transfer into high refractive index TiO₂.^[28,29] Similar to the approach by Donie et al., the nanodisk arrays are planarized by a polymer layer to provide a flat substrate for the subsequent deposition of the electrically active layers, ensuring stable electrical characteristics of the device. The resulting thin, compact scattering layer is intended as an internal out-coupling structure to address the

issue of losses through thin film waveguide modes in OLEDs. As we will show, the structures additionally function as an out-coupling layer for substrate modes. As a model system, we fabricate monochromatic OLEDs ($\lambda_0 = 520$ nm), however, our findings should also be applicable to white OLEDs. The nanodisks are arranged in a correlated disorder configuration, ensuring on the one hand structural correlations that are beneficial to the scattering properties, and on the other hand in-plane isotropy.^[30,31] Hence, the emission patterns are invariant with respect to the azimuthal angle and do not introduce unwanted effects such as butterfly-like emission patterns. Based on our experimental findings, we include an in-depth numerical analysis where we focus on the properties of the individual scatterer, and make suggestions on improving the latter.

2. Results

The following main part of the paper (Sections 2 and 3) starts with a numerical analysis of the losses through waveguide modes within the OLED layer stack specific to the anticipated device configuration. Next, the concept of planar substrates with integrated disk-shaped high index scattering elements is introduced, which serves as basis for the fabrication of monochromatic OLEDs. The substrates and devices are characterized both optoelectronically and optically, followed by a numerical analysis of the scattering structure in Section 3.

2.1. Losses through Waveguide Modes

Our first aim is to characterize waveguide mode losses specific to our device architecture. As the layer stack is deposited with identical parameters as in a previous work by Donie et al.,^[27] its composition, electronic function, and layer thicknesses are well known (see Section 5 for details). A schematic representation of the layer stack, including the refractive indices n used for calculations at a later stage, is presented in **Figure 1** (left). Since the respective refractive indices of the organic layers (MTDATA and BPhen) are nearly identical, we combine them into one layer for the following optical analysis.^[32,33] Furthermore, all layers except the aluminum back reflector are assumed to be non-absorbing. Optically, the layer stack constitutes a waveguide structure, for which we solved the eigenvalue equation and found the three eigenmodes j (TE₀, TM₀, and TM₁), that are shown as intensity profiles in **Figure 1** (right, see numerical methods in Experimental section for details on the calculation). Due to absorption in the aluminum, the effective refractive index $n_{\text{eff},j}$ is generally a complex number (**Table 1a**), from which we can calculate an effective absorption coefficient $\alpha_{\text{abs},j} = 4\pi/\lambda_0 \text{Im}\{n_{\text{eff},j}\}$ for each mode. $\alpha_{\text{abs},j}$ characterizes the intensity decay of the mode per propagation length (μm traveled). The attenuation is particularly strong for TM₀, which we identify as a surface plasmon polariton (SPP) mode.

Exemplary emitter molecules in **Figure 1** are placed right in the center of the Ir(ppy)₃ containing layers and are modeled as dipoles (see numerical methods). The overlap of the dipole fields with the respective eigenmode j defines the coupling efficiency $\eta_{dp,j}$ between the two (**Table 1a**). Taking into account

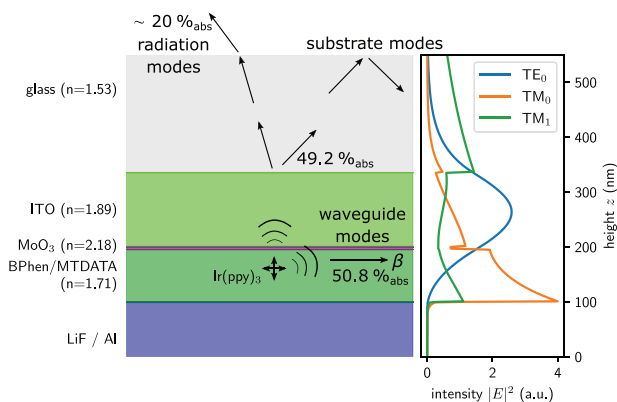


Figure 1. Left: Schematic cross-section of the OLED devices discussed throughout this study. The doped organic layers are actually stratified layers of the two materials BPhen and MTDATA, but treated as one layer for the numerical work in this study, as the refractive indices are close. Of the power emitted by the Ir(ppy)₃ molecules (randomly oriented, center wavelength $\lambda_0 = 520\text{ nm}$), 49.2%_{abs} are transmitted to the substrate of which $\approx 20\%$ _{abs} are transmitted to radiation modes.^[1] The remaining 50.8%_{abs} propagate as waveguide modes with propagation constant β (calculated on a computational domain of $R_{CD} = 3000\text{ nm}$, $H_{CD} = 1500\text{ nm}$, see numerical methods section). Right: Specific intensity profiles for the waveguide modes across the height z .

$\eta_{dp,j}$ for every mode, according to our calculation, only 49.2%_{abs} of the total emitted dipole power is emitted into the substrate.^[34] The remaining 50.8%_{abs} propagate as waveguide modes along the thin film stack, which is in line with estimates from previous studies.^[1] Though it is not the focus of this publication, it is worth noting that for a flat glass substrate about 30%_{abs} are trapped in the substrate and only about 20%_{abs} is estimated to be emitted to the surrounding in radiation modes.^[1]

2.2. Substrates with Integrated Scattering Structure

It is favorable to decouple the optical from the electronic functionality of an optoelectronic device. In case of OLEDs, electronically active layers should ideally be planar for the ease of OLED stack processability and hence reproducibility of electrical performance, while optical scattering occurs at corrugated surfaces. To combine these seemingly opposed demands, we chose to embed high refractive index optical scatterers within a transparent layer to maintain a planar surface. For our OLED device configuration, this approach is shown in **Figure 2a**, where patches of higher index material are integrated into the substrate close to the OLED layer stack. Similar to a waveguide grating coupler, a mode with propagation constant $\beta = |\beta|$ is scattered at this structure, $\beta \rightarrow \mathbf{k}_{\text{sub}}$ thereby enabling coupling between waveguide and substrate modes. This process represents an additional decay channel with constant $\alpha_{\text{sca},j}$. In total, the decay of the waveguide mode j is then described by Lambert's law

$$I(r) = I_0 e^{-(\alpha_{\text{sca}} + \alpha_{\text{abs}})r} \quad (1)$$

for propagation along a spatial coordinate r . For each scattering element, we can define a (1D) scattering cross-section $C_{\text{sca},j}$ for our waveguide structure, that is directly linked to the scattering coefficient via $\alpha_{\text{sca},j} = \rho C_{\text{sca},j}$, where ρ is the density of scatterers per unit area.^[35] In doing so, we implicitly assume that each element scatters independently and correlations in between disks on average cancel out.

For an unperturbed, planar waveguide the scattering contribution is $\alpha_{\text{sca}} = 0$ and the mere coupling of the dipole to the waveguide is a loss path, whereas any out-of-plane scattering will enhance the emission efficiency. Consequently, we need to

Table 1. Parameters of waveguide modes j within the OLED thin film stack. a) Unperturbed waveguide: Effective refractive indices $n_{\text{eff},j}$, absorption coefficient $\alpha_{\text{abs},j}$, and coupling efficiency $\eta_{dp,j}$ to an isotropic point source within the stack. b) Experimental geometry: Scattering cross-sections $C_{\text{sca},j}$, extraction efficiencies $\eta_{\text{ext},j} = \alpha_{\text{sca},j} / (\alpha_{\text{abs},j} + \alpha_{\text{sca},j})$ and propagation lengths α_j^{-1} for the relevant waveguide modes and for nanodisk dimensions as shown in Figure 6. c) Improved geometry: The same quantities, but with nanodisks placed directly onto the OLED stack (see Figure 8), and extraction efficiency and propagation lengths calculated for the highest possible packing density of a random sequential adsorption (RSA) pattern.

		Mode j			
		Quantity	TE ₀	TM ₀	TM ₁
a)	Unperturbed waveguide	$n_{\text{eff},j}$	$1.70 + 9.98 \times 10^{-4}i$	$1.82 + 1.71 \times 10^{-2}i$	$1.53 + 3.77 \times 10^{-3}i$
		$\alpha_{\text{abs},j} [\mu\text{m}^{-1}]$	0.0241	0.4122	0.0911
		$\eta_{dp,j}$	0.0834	0.3760	0.0486
		$\sum_j \eta_{dp,j}$		0.508	
b)	Experimental geometry	$C_{\text{sca},j} [\text{nm}]$	5.6	2.9	331.4
		$\eta_{\text{ext},j}$	0.287	0.012	0.848
		$\alpha_j^{-1} [\mu\text{m}]$	29.5	2.4	1.5
c)	Improved geometry	$C_{\text{sca},j} [\text{nm}]$	361.4	64.6	411.5
		$\eta_{\text{ext},j}$	0.982	0.363	0.936
		$\alpha_j^{-1} [\mu\text{m}]$	0.75	1.55	0.63

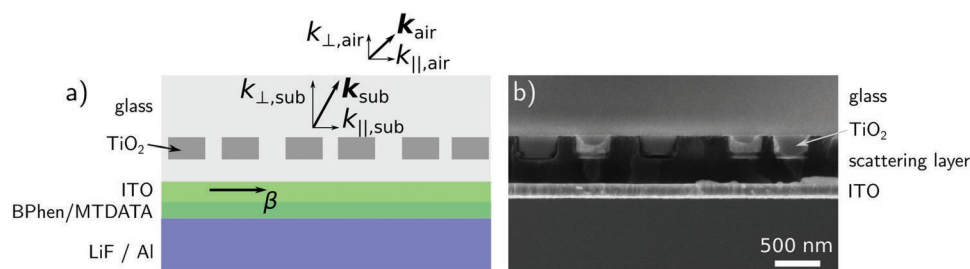


Figure 2. a) Schematic illustration of the device cross-section with substrate integrated, disk-based scattering structure (MoO₃ is not shown, see Figure 1). Waveguide modes propagate with constant β , are scattered at the disks to substrate modes with \mathbf{k}_{sub} and to radiation modes with \mathbf{k}_{air} , if the parallel component $k_{\parallel,\text{sub}}$ is sufficiently small. b) Cleaved edge of substrate with integrated disks and ITO contact layer below before deposition of organic layers.

consider the relationship of the competing processes scattering and absorption, or to express the efficiency of a scattering structure as a single figure of merit,

$$\eta_{\text{ext},j} = \alpha_{\text{sca},j} / (\alpha_{\text{sca},j} + \alpha_{\text{abs},j}) \quad (2)$$

for each mode j . Since we consider the electronic device architecture and hence $\alpha_{\text{abs},j}$ for the most part unalterable for the design envisioned in Figure 2, we shall henceforth focus on increasing $\alpha_{\text{sca},j}$.

High refractive index, disk-shaped scatterers exhibit exceptionally strong scattering efficiencies and are therefore well known building blocks in nanophotonic structures. Compared to spherical scatterers with radius R , they possess an additional degree of freedom of design with the height H , such that electric and magnetic resonances can, to some degree, be tuned individually. In a recent experimental work,^[29] we demonstrated strong scattering at TiO₂ nanodisks ($n = 2.45$ at $\lambda_0 = 520$ nm, see Figure S1, Supporting Information, for optical properties) in the range from $\lambda_0 = 500$ to 600 nm, and therefore fabricated a similar nanodisk pattern for the current study (see Experimental Section for fabrication details).

We achieved a disordered pattern of random sequential adsorption-type (RSA) of nanodisks of dimensions $R = 219$ nm and $H = 199$ nm (Figure 3a). The size dispersion of ± 10 nm with respect to R was estimated from the size dispersion of the PMMA colloids^[36] that were used as templates. Additionally, a minority of larger, non-cylindrical particles occur due to aggregation of colloids. The size dispersion in H is negligible due to the excellent homogeneity of the atomic layer deposited TiO₂. The nanodisk density is $\rho \approx 1.72 \mu\text{m}^{-2}$, which is equivalent to an area fill fraction of $\phi \approx 0.260$. The nanodisks were then

embedded in a spin-coated layer of SU-8 photoresist (450 nm thickness), providing a planar interface for the subsequent deposition of the first electrically relevant layer (indium tin oxide, ITO), as shown under oblique viewing angle in Figure 3b. The refractive indices of photoresist ($n \approx 1.56$) and soda-lime glass substrate ($n \approx 1.53$) at $\lambda_0 = 520$ nm are sufficiently similar, such that we treat them as the same material (with $n \approx 1.53$) for any calculations at a later stage of the manuscript. In a cross-section view, we thereby achieve the desired configuration of the previously proposed waveguide outcoupling structure (Figure 2a,b).

2.2.1. Optoelectronic Properties

We used these substrates to fabricate green OLEDs (with center wavelength $\lambda_0 = 520$ nm) using the same parameters as described in ref. [27]. Additionally, we fabricated a series of reference devices on substrates, that have been coated with the same photoresist used for planarization, but omitting the nanodisk fabrication (see Figure S2, Supporting Information, for additional reference devices on bare glass substrates). The typical current-voltage characteristics for both OLED types (scattering and non-scattering substrates) are almost identical (Figure 4a), since all devices comprise the same layer stack. Only at sub-threshold voltages below around 2.5 V we observe slightly higher leakage currents for the scattering substrates. However, the observed values of $< 10^{-4}$ mA cm⁻² (Figure 4a, inset), are typical for other flat substrates and as such are not considered problematic.^[22,37]

The overall effectiveness of a light-coupling structure is best assessed by the increase in EQE (Figure 4b). The highest

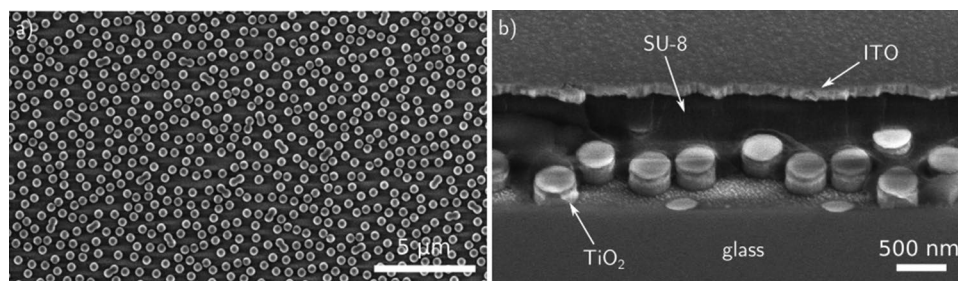


Figure 3. a) Top view of the fabricated array of identical nanodisks with dimensions $R = 219$ nm and $H = 199$ nm. b) Nanodisks embedded in a layer of SU-8 resist and coated with ITO, that serves as contact layer of the subsequently fabricated OLED stack.)

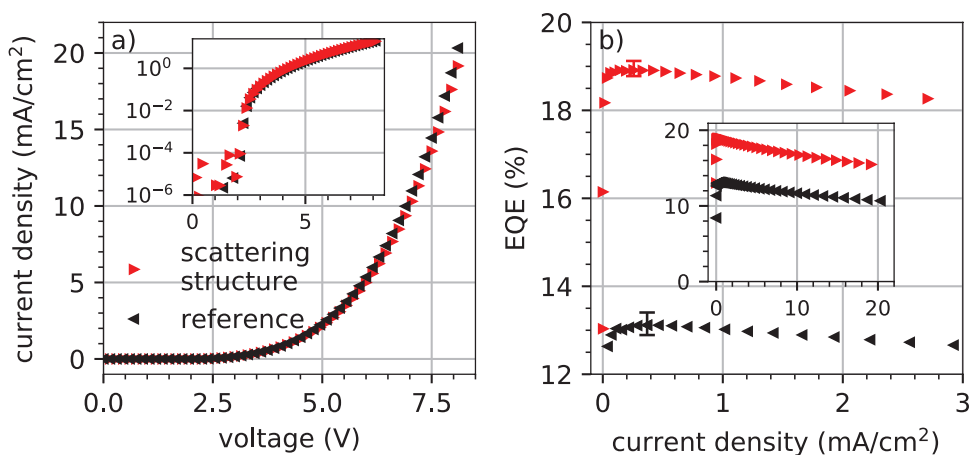


Figure 4. Optoelectronic properties of OLED devices with integrated scattering structure and of unstructured references. a) Current density versus voltage in linear and logarithmic representation (inset). b) External quantum efficiency (EQE) versus current density. All data are averages over four devices of 0.09 cm^2 active area each. The error bars span over the absolute range of all measured values. Axis labels are also valid for the inset, respectively.

EQEs of 13.1% (non-scattering) and 18.9% (scattering substrate) for both substrate types are achieved at low current densities around 0.4 mA cm^{-2} , respectively. In relative terms, this is equivalent to a 44.2%_{rel} increase due to the substrate integrated scattering structure. Note also, that the presented data are mean values of four devices with identical configurations for each type and the deviation from the mean in absolute terms is rather small, thereby demonstrating the robustness that is a consequence of the planarization. Though we here only present the data for the best performing set of device parameters, we observed this robustness at a larger number of samples with scattering substrates fabricated with the same technique. In contrast, an experiment with corrugated substrates (see Figures S3 and S4, Supporting Information) produced a higher rate of failure and large variety of values for EQEs, which is in line with the observations of other researchers.^[17]

2.2.2. Spectral and Angular Response

First, we assess the response of the scattering substrates, for which we provide transmittance (total and diffuse) and reflectance spectra (Figure 5a). Again, as for the optoelectronic measurements above, we use a photoresist coated glass substrate (without nanodisks) as reference, where T_{ref} is in the range from $\approx 89\%$ to 91% from $\lambda_0 = 400$ to 700 nm . As the refractive indices of glass and photoresist are very similar, we observe only a minor wavelength dependence due to thin film resonances.

For the scattering substrate (Figure 5a), the transmittance T fluctuates around 78% throughout the measured spectrum, while reflectance R fluctuates around a mean value of 16%. The wavelength dependence is a consequence of Mie resonance, as we discussed in great detail in a previous work.^[29] However, the refractive index contrast between glass/photoresist and nanodisks is small compared to the structures in ref. [29], hence the features in the spectrum are not as pronounced. The remaining share of the incident light, $1 - T - R$, includes losses through substrate modes that are emitted at the edges of the

substrate and hence not detected, and potentially absorption. However, since the here used SU-8 photoresist and the TiO_2 nanodisk material are only weakly absorbing in the measured wavelength regime, we expect absorption to be negligible.

The diffuse share of transmittance T_{diff} ranges from around 60% at $\lambda_0 = 400 \text{ nm}$ to 10% at $\lambda_0 = 700 \text{ nm}$. Accordingly, the haze reaches values of up to 79%, which is comparable to volumetric scattering layers of multiple μm thickness. However, the latter is usually accompanied by a drop in total transmittance, which for our structure, in contrast, remains rather high.^[22,27]

Next, we focus on the angular and wavelength resolved emission of an OLED on a scattering substrate compared to the reference (Figure 5b,c). At small angles (0° and 20°) the spectrum hardly differs for the scattering substrate, while the emission intensity drops significantly in case of the unstructured reference. To show this more clearly, we calculated the angle resolved emission intensity integrated over the full spectrum (polar representation in Figure 5d). Compared to Lambertian emission, the emission of the reference device drops more quickly with increasing angle, while the scattering substrate leads to enhanced emission in larger angles. A similar representation for specific wavelengths (at $\lambda_0 = 520$ and 542 nm) shows that the emission enhancement at larger angles is wavelength dependent (Figure 5e,g, respectively). For instance at $\lambda_0 = 520 \text{ nm}$ and 45° angle, the normalized intensities are 0.52 versus 0.76 (reference vs scattering substrate), that is an increase of 46%. At $\lambda_0 = 542 \text{ nm}$, in contrast, the most pronounced difference is $\approx 34\%$ at around 30° .

3. Discussion

For further insights into the perturbation of the waveguide modes by an individual nanodisk and the performance of the scattering structure, we discuss the experimental results thoroughly through numerical analysis. Based on our approach, we evaluate options to further improve the performance of internal scattering structures.

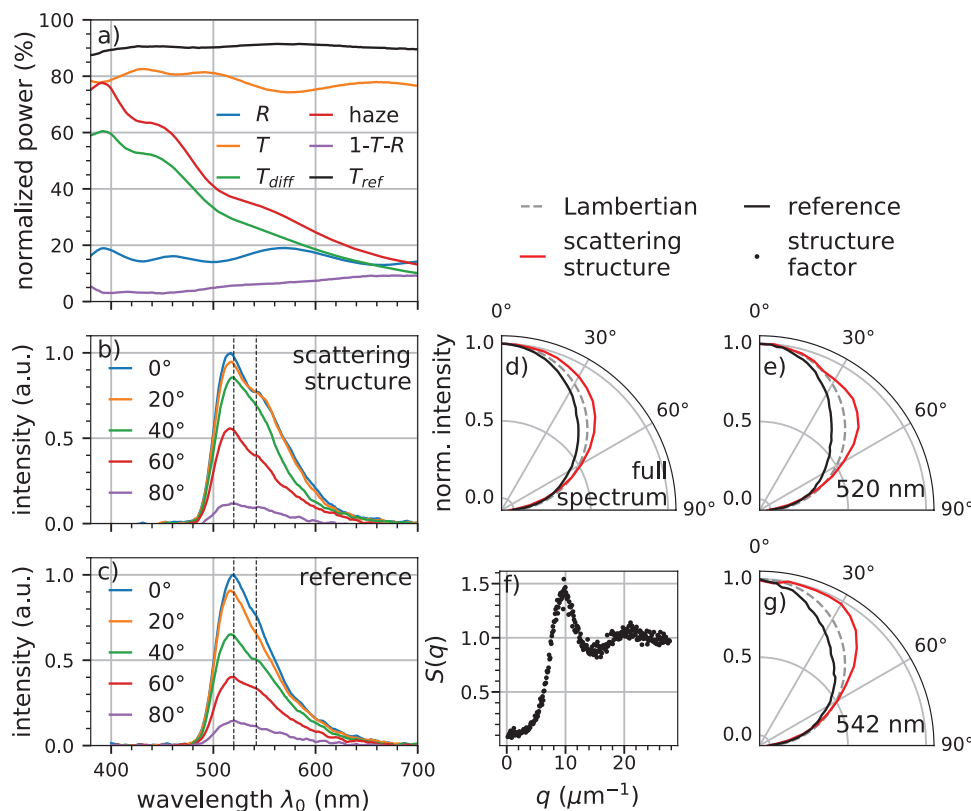


Figure 5. a) Optical properties of the planarized nanodisk scattering structure. Total reflectance R and transmittance T , diffuse share of transmittance T_{diff} . Total transmittance T_{ref} of a flat glass substrate coated with 400 nm SU-8 photoresist. b,c) Emission spectra versus vacuum wavelength λ_0 depending on viewing angle (polar) for OLED device with scattering structure and unstructured reference. d,e,g) Polar representations of emission profiles averaged over the full spectrum and selected wavelengths, respectively, each normalized to emission intensity at 0° . f) Structure factor of the nanodisk pattern.

3.1. Coupling and Scattering

The following results were obtained from 3D FEM simulations on a cylindrical computational domain similar to the one in Figure 11, with the individual nanodisk centered above the OLED layer stack. The nanodisks were assumed to be non-absorbing ($n = 2.45$ at $\lambda_0 = 520$ nm) and all dimensions were chosen as determined in the experiment. Since the area covered with TiO_2 nanodisks is only about $\phi \approx 0.26$, we assumed that most of the emitted power is either directly coupled into propagating substrate and air modes or into waveguide modes (see Section 2.1). Hence, instead of dipole sources, we here used a unidirectional waveguide mode of the respective type to excite the individual nanodisk.

The near- and far-field intensities are presented in Figure 6a,b, respectively. Along the left edge of each nearfield images, the color-coded mode profiles (see also Figure 1) can be identified. However, for TM_1 the highest intensity is found within the nanodisk or in its direct vicinity.

The high intensity near the nanodisk suggests strong TM_1 mode coupling to localized modes of the nanodisk. In contrast, coupling is barely visible in the nearfield image for TE_0 and TM_0 , presumably since the fields of those modes are more concentrated in the thin film stack and do not reach as far out into the substrate.

The far field intensity for all three modes, respectively, is directed to shallow angles with respect to the propagation direction (Figure 6b). By integrating over power scattered into the far field and comparing to the incident mode intensity, we can calculate the scattering cross-section C_{sca} of the nanodisk for each mode (Table 1b). Since each mode is arbitrarily extended in one lateral direction, C_{sca} is a 1D quantity in this case. In particular, for TE_0 and TM_0 the scattering cross-section is small compared to the geometrical cross-section $2R = 438$ nm. Note, that scattering can also occur to other modes, that is mode coupling through disks. However, according to our calculations the converted power is about two orders of magnitude smaller than the far field emission, and we therefore only consider scattering to the far field.

As pointed out at Equation (1) (above), scattering should only be assessed relative to absorption, or as a single measure of mode extraction efficiency $\eta_{ext,j}$ (Equation (2)). Due to the relatively small absorption losses for TE_0 (see Table 1a), we observe significant $\eta_{ext,j}$ even though C_{sca} is small (Table 1b). This is not the case for TM_0 , where significant absorption losses in combination with a small scattering cross-section leads to a minuscule extraction efficiency of about 0.012. The strongest efficiency is achieved for TM_1 , where the combination of C_{sca} (large) and α_{abs} (small) is favorable.

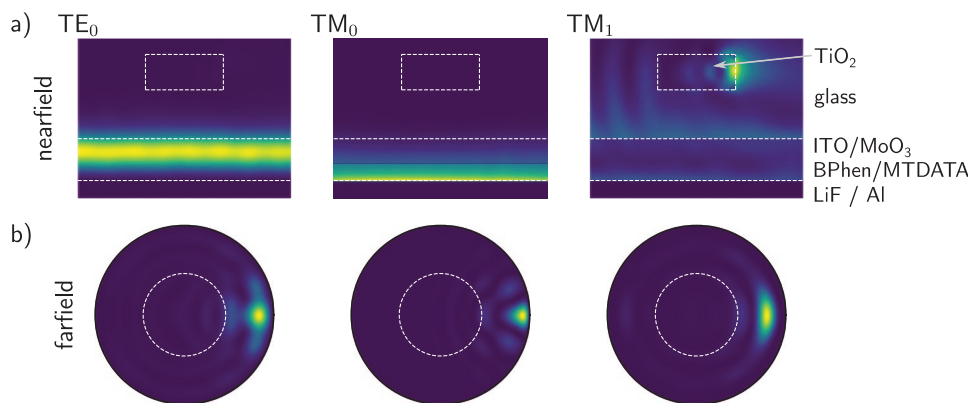


Figure 6. a) Nearfield intensities at cross-section through the center of the nanodisk along the direction of the propagating modes from left to right, respectively. The dashed contours mark the thin film stack (excluding aluminum) and the TiO₂ nanodisk with dimensions $R = 219$ nm and $H = 199$ nm embedded in the substrate. b) Projected far field intensities of scattered radiation by the nanodisks. The dashed circle marks the angle of total internal reflection at the glass substrate's front surface.

Comparing Table 1a and b, the extraction efficiency $\eta_{\text{ext},j}$ is lowest for the modes with the strongest excitation (high $\eta_{\text{dp},j}$). Hence, the anticipated recovered power from waveguide modes is only $\sum_j \eta_{\text{dp},j} \eta_{\text{ext},j} \approx 7.0\%_{\text{abs}}$, thereby changing the dipole power emitted to substrate modes from $49.2\%_{\text{abs}}$ to $56.2\%_{\text{abs}}$. Comparing this to the unstructured base case where about $20\%_{\text{abs}}$ of the emitted power is coupled to radiation modes,^[1] this would result in a EQE increase of only $\approx 35\%_{\text{rel}}$, instead of the measured $44.2\%_{\text{rel}}$. This estimate is based on assuming perfect coupling of the additionally recovered power from waveguide modes to radiation modes. Considering the far field emission into shallow angles (Figure 6) this is a rather keen assumption. However, the nanodisk structure does not only scatter waveguide modes, but also light that is trapped in the glass substrate. Even in a flat OLED device configuration with no scattering into oblique angles by a nanostructure, these substrate modes typically account for $\approx 30\%_{\text{abs}}$ of the efficiency losses,^[1] thereby offering the perspective of more than doubling the EQE by substrate mode extraction alone. In the following,

we continue to disentangle the effects of waveguide mode and substrate mode extraction.

3.2. Dispersion Diagram

In the dispersion diagram in Figure 7, the green line marks photon energy corresponding to the design wavelength of $\lambda_0 = 520$ nm. The filled circles on the right end of the line mark the propagation constants β_j of the previously identified modes.

Since $k_{\parallel} \leq k$, no light can propagate beyond the respective light line (blue) in air. Hence, the transition from waveguide modes (filled circle) to radiation modes (triangle Δ) requires an additional contribution Δk_{\parallel} (upper curved arrow). If a coherent wave (mode) propagates for a sufficient distance α^{-1} within the thin film stack, this change in momentum can be provided by coherent scattering through structural correlations in the nanodisk pattern. The latter are best expressed by the structure factor $S(q)$ which exhibits a peak at q_0 (see Figure 5f) and for the sake of this discussion we assign $\Delta k_{\parallel} = q_0$ in Figure 7. Accordingly, the parallel component of the wavevector is changed to $k_{\parallel} \approx \beta - q_0$ and “direct” out-coupling of the waveguide to radiation modes (triangle Δ) can occur, for which we would expect an emission angle of 64° for TE₀ (top horizontal axis in Figure 7).

Given the values for α_j^{-1} and extraction efficiencies, this process may be significant primarily for TE₀, and less so for the other modes where propagation lengths are rather short. However, as a first order approximation, the individual disks far field emission pattern and the scattering pattern defined by the structure factor are multiplicative,^[29] which makes this process less likely even for TE₀. On a side note, this aspect has implications also for the extraction efficiencies (see Equations (1) and (2)) which have thus far been calculated assuming negligible correlations, as would be the case for a fully disordered pattern. Note further, that these implications become even more relevant for example, a periodic pattern, where $S(q) = 0$ for all q except for Bragg peaks. A more detailed consideration of the structural correlations would require to model the interplay of $S(q)$, individual disk's farfield response and propagation length

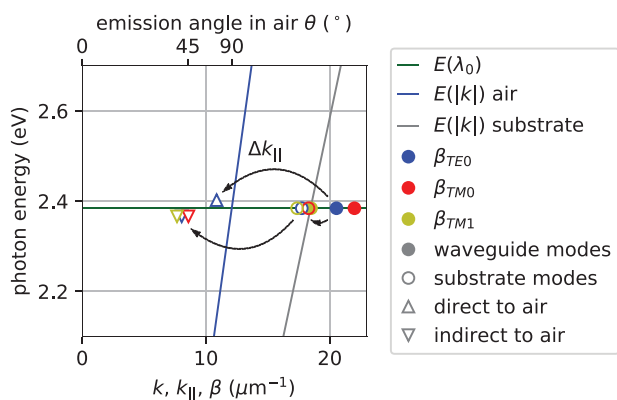


Figure 7. Dispersion relation $E(k = |\mathbf{k}|)$ in substrate and in air, respectively, photon energy $E(\lambda_0)$ at design wavelength $\lambda_0 = 520$ nm and propagation constants β_j for each waveguide mode j . The parallel components $k_{\parallel,j}$ in the respective medium are plotted as open symbols, and the potential directional changes through Δk_{\parallel} are marked with arrows.

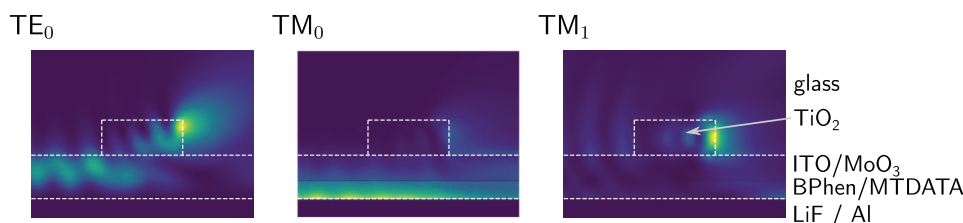


Figure 8. Nearfield intensities at cross-section through the center of the nanodisk along the direction of the propagating modes from left to right, respectively. The nanodisks dimension is identical to Figure 6a, however, it is now placed directly on top of the OLED stack.

in order to obtain the farfield response of the entire structure, which is beyond the scope of this work.

If, as the desired strong scattering implies, propagation lengths α_j^{-1} are short compared to the typical correlation lengths $2\pi/q_0$ of the disk pattern, scattering is dominated by the single disk's response and correlations are of no importance. From the scattering directions of 74° , 82° , and 70° for TE_0 , TM_0 , and TM_1 (angles of highest far field intensity within the substrate in Figure 6b), we can infer the corresponding parallel components of the wavevectors within the substrate (open circles in Figure 7). Since all open circles are found between the light lines for air and substrate, that is, light is trapped in the substrate, an additional change in k_{\parallel} is needed for propagation in air. This change in momentum can either be provided by a scattering structure at the substrate-air interface, or, as in our case, the waveguide modes are scattered again at the substrate integrated nanodisk structure near the OLED stack. Since the propagation lengths in the non-absorbing substrate are long, scattering is heavily influenced by the structure factor, that is, $\Delta k_{\parallel} \approx q_0$. The anticipated k_{\parallel} and emission angles in air of 42° , 45° and 39° (for TE_0 , TM_0 , and TM_1 , respectively) are plotted as inverted triangles in Figure 7. The transition from waveguide to radiation modes occurs in two steps and may hence be dubbed "indirect."

In any case, both possible extraction paths, direct and indirect, would place the expected emission angles in line with the experimental observations of enhanced emissions in the 30° to 65° range (Figure 5d). To fully disentangle the effects of waveguide mode and substrate mode extraction by a structure such as ours would require measurements of output power with an ideal outcoupling structure for the substrate modes.

3.3. Improved Scattering Structures

In the following section, we will numerically evaluate a number of approaches to improve the functionality of the internal outcoupling structure. Note, that we focus only on dipole emission coupled to substrate modes (propagating in the glass substrate), rather than to radiation modes (in air). Substrate-to-radiation mode coupling is achievable irrespective of the design of the electrically active layer and therefore not within our quest to design effective internal outcoupling structures.

3.3.1. Disks Close to Waveguide

As pointed out above, the rather low extraction efficiencies are due to the poor coupling of the nanodisks to the waveguide

modes (Figure 6). In a first approach to improve the internal scattering structure, one could place the nanodisks directly on top of the OLED stack. Scattering of all three waveguide modes at the nanodisk is apparent in the respective nearfield intensities (Figure 8). For TE_0 and TM_1 the highest intensity is found in the vicinity of the disk. For TM_0 the highest intensity is still found within the OLED stack, however, the decay along the propagation direction (left to right) indicates significant interaction of the waveguide mode with the disk.

By integrating over the far field (for intensity distribution see Figure S5, Supporting Information), we obtain the scattering cross-section C_{sca} (Table 1c), which provides a single figure of merit for each mode to assess the scattering at the disk. Scattering is greatly increased compared to the experimentally achieved geometry, particularly for the TE_0 and TM_0 mode.

3.3.2. Maximized Disks Density

A second approach to improving the internal scattering structure is to increase the density and hence area fill fraction of the nanodisks from the experimentally achieved $\phi \approx 0.260$ to the saturation density of the proposed RSA pattern of $\phi \approx 0.547$.^[38] Taking into account the increased disk density and the scattering cross-section of the disk close to the waveguide, for each mode j we can calculate the extraction efficiency $\eta_{ext,j}$ (Table 1c).

Compared to the experimentally achieved geometry, the extraction efficiency is increased $3.4\times$ for TE_0 and $30\times$ for TM_0 , while only a slight change occurs for TM_1 . Taking into account the dipole coupling efficiency to each mode $\eta_{dp,j}$ we can calculate the potential for power recovery $\sum_j \eta_{dp,j} \eta_{ext,j} \approx 20.3\%_{abs}$ through waveguide mode outcoupling, which is an almost $3\times$ increase compared to the calculation based on the experimentally achieved design. The emitted dipole power to substrate modes thereby increases from $1 - 0.508 = 49.2\%_{abs}$ (Table 1a, unperturbed waveguide) to $49.2\%_{abs} + \sum_j \eta_{dp,j} \eta_{ext,j} \approx 69.5\%_{abs}$.

Note, that this calculation is based on the assumption of increased scattering of waveguide modes (see Section 3.1, Supporting Information). For higher disk densities, however, another effect could gain importance: A dipole emitter may also directly excite photonic resonances in a nearby nanodisk,^[29] potentially modifying the emitters radiative decay channel, for example leading to superradiant emission. Though this aspect is beyond the scope of the work at hand, we believe that following up into this direction in future investigations will

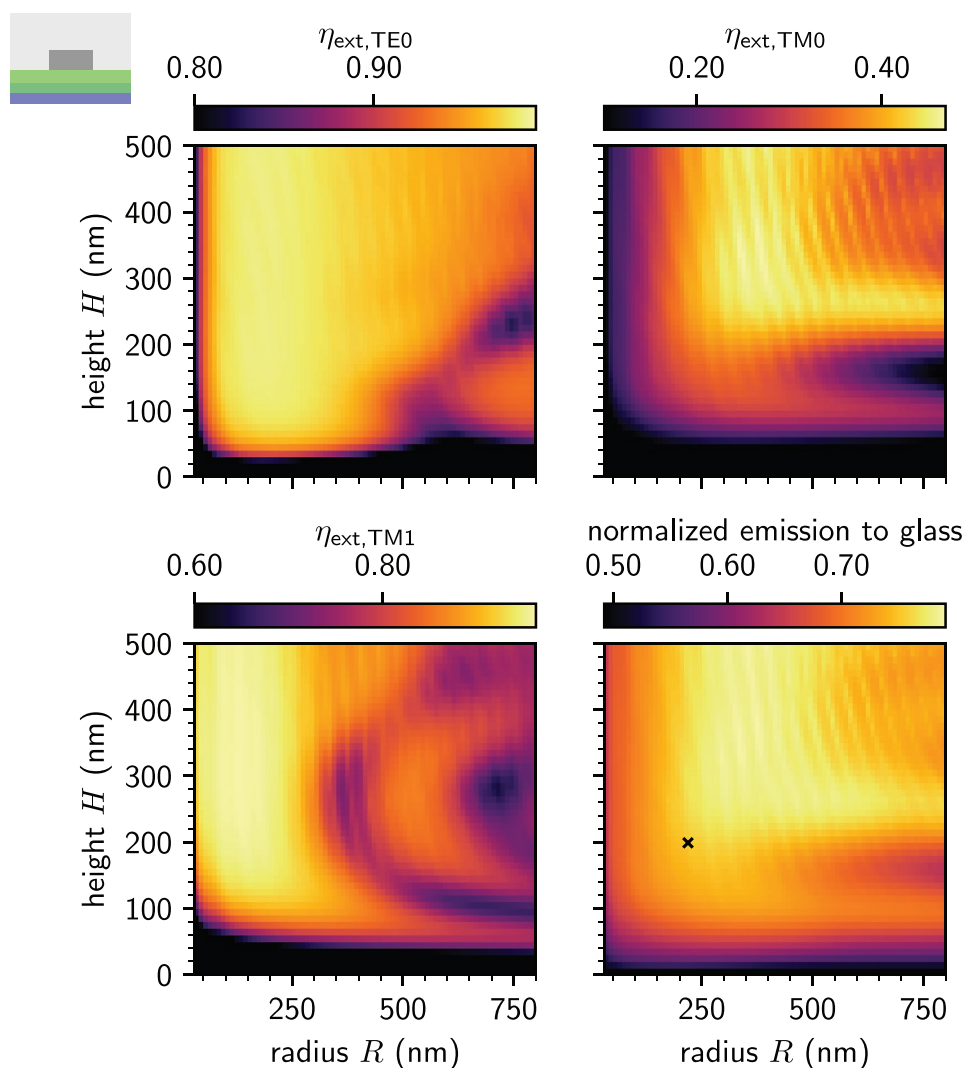


Figure 9. Extraction efficiencies $\eta_{\text{ext},j}$ of modes j for various disk sizes R , H at the highest possible surface fill fraction for RSA patterns and disks placed directly onto the OLED stack (top left sketch, see Figure 2a for color-coded materials). Bottom right: Share of emitted dipole power that propagates in the glass substrate. The experimentally achieved disk dimensions at $R = 219$ nm and $H = 199$ nm are marked (x). All calculations were carried out on a computational domain of $R_{\text{CD}} = 1000$ nm, $H_{\text{CD}} = 1000$ nm.

prove scientifically fruitful and valuable. Furthermore, it remains an important and closely related question, if a scattering element that acts as a good outcoupler for waveguide modes also couples well to a dipole emitter in its direct surrounding, that is, if an optimization for both coupling effects lead to the same scattering element.

3.3.3. Optimized Disk Dimensions

A third approach to increasing extraction efficiencies is to optimize the individual nanodisks dimensions. To evaluate this option, we calculated the extraction efficiencies $\eta_{\text{ext},j}$ for ≈ 5000 different nanodisks ranging from height $H = 1$ nm to $H = 500$ nm, and from radius $R = 1$ nm to $R = 800$ nm (Figure 9). The area fill fraction is kept constant at $\phi = 0.547$, which implies that the number density scales $\propto R^{-2}$. Since the normalized

power carried by each mode is known (Table 1a), we can use $\eta_{\text{ext},j}$ to calculate the total emission to glass $49.2\%_{\text{abs}} + \sum_j \eta_{\text{dp},j} \eta_{\text{ext},j}$ (Figure 9, bottom right).

For TE_0 , $\eta_{\text{ext},\text{TE}_0}$ is robust with respect to size variations, however, $\eta_{\text{ext},\text{TE}_0}$ is significantly smaller for $H \lesssim 70$ nm, and shows a slight reduction for some combinations of R (large) and H (small). The case is similar for TM_1 , where $\eta_{\text{ext},\text{TM}_1}$ for small R is invariant with respect to H above ≈ 80 nm, but shows some H dependence for larger R . In contrast, TM_0 , $\eta_{\text{ext},\text{TM}_0}$ changes more drastically with respect to the dimensions, with the highest value at $R \approx 370$ nm and $H \approx 370$ nm. Neither larger R nor larger H lead to an increase of $\eta_{\text{ext},\text{TM}_0}$, and the combination of even larger R and H even leads to a reduction.

The lowest normalized emission to glass (Figure 9, bottom right) is again $49.2\%_{\text{abs}}$ for the unperturbed waveguide (no disks, $H = 0$ nm). The overall size dependence is similar to, albeit less pronounced than for $\eta_{\text{ext},\text{TM}_0}$. This is not surprising,

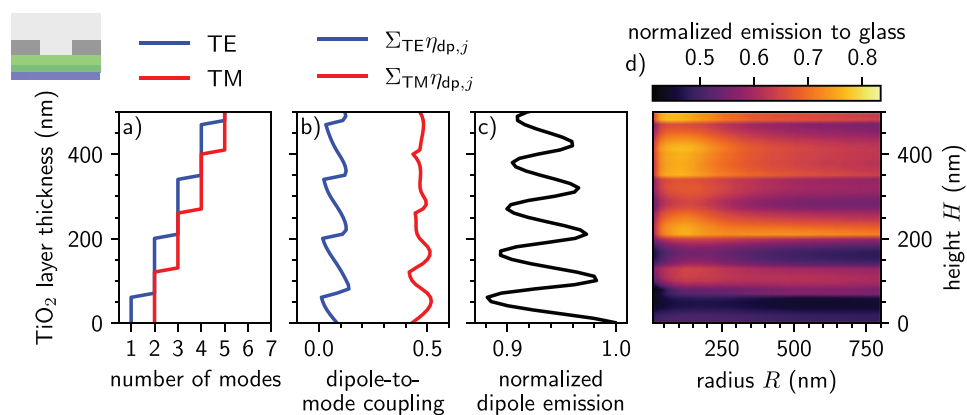


Figure 10. Notch in TiO₂ layer design (top left sketch, see Figure 2a for color-coded materials). a) Number of modes versus layer thickness in the thin film stack if a layer of TiO₂ is added to the OLED stack. b) Sum of coupling efficiencies of dipoles to TE and TM modes. c) Average emission of a randomly oriented dipole normalized to emission without TiO₂ layer. d) Dipole emission to the glass substrate normalized to the dipole power without TiO₂ layer. All calculations were carried out on a computational domain of $R_{CD} = 1500$ nm, $H_{CD} = 1500$ nm.

since TM₀ is the mode with the strongest excitation and η_{ext, TM_0} is more clearly size dependent than η_{ext, TE_0} and η_{ext, TM_1} . The latter are relatively large for most disk dimensions in Figure 9 and leave little room for improvement. Consequently, the potential for improvement compared to the previously discussed (and experimentally achieved disk dimensions, marked in Figure 9, bottom right) is mostly given through improvements for TM₀. The highest value of about 79.1%_{abs} is found at $R \approx 330$ nm and $H \approx 350$ nm, however, at $H \approx 220$ nm the normalized emission to glass is already 76.8%_{abs} and relatively independent of R for larger R . Even a slight increase of the experimentally achieved R and H would therefore place the disk size in this near-optimum, robust size regime.

Once $R \gtrsim 600$ nm, η_{ext, TM_0} shows local maxima that are relatively insensitive to R at $H \approx 100$ nm and $H \approx 240$ nm (Figure 9). Arbitrarily large disks, that is, an extended layer of TiO₂, must be considered as part of the waveguide structure. Though at $R = 600$ nm, the disk diameter $2R$ is only approximately six times the wavelength in TiO₂, we probably start to see this effect in η_{ext, TM_0} : The guided modes of the OLED stack are coupled to the eigenmodes of the altered stack (including the TiO₂) layer and coupled to glass where the layer (i.e., the large disk) ends.

3.3.4. Inverted Disk Structure

To address this issue, we recalculated the dipole-to-waveguide mode coupling and emission to glass for an inverted TiO₂ structure, that is, an extended TiO₂ layer with circular notches instead of TiO₂ disks (Figure 10). TiO₂ being part of the waveguide implies a different set of TE and TM eigenmodes, the number of which are determined by the thickness of the TiO₂ layer and are presented in Figure 10a. The base case from above is included at $H = 0$ nm, where only one TE and two TM modes are present due to the OLED stack. With increasing H , the number of TE and TM modes increases by turns.

Similar to before, we calculated the average coupling efficiency $\eta_{dp,j}$ of an arbitrarily oriented dipole to those modes. However, as the number of modes can get rather large, we only present the respective sum for TE and TM (Figure 10b), that is,

the loss through those modes if not recovered by a scattering structure. Note also, that the test dipoles are now placed underneath the TiO₂ layer. For large disk and high disk density this is commonly the case since the emitter molecules are laterally evenly distributed. Different from previous disk-type setup, where dipole-to-mode coupling was determined for the original OLED stack waveguide, we now also need to take into account that dipole emission may be influenced by the TiO₂ layer, that is, the Purcell factor changes, as shown normalized by the base case with no TiO₂ layer in Figure 10c. This aspect was previously not covered in simulations for the disk-type design.

Whenever the number of modes for the respective type (TE or TM in Figure 10a) increases, the coupling to this type of mode increases at the cost of the other (Figure 10b). The dipole emission normalized by the base case (Figure 10c) shows an oscillating behavior with respect to H , but the strongest emission is still found if no TiO₂ layer is present ($H = 0$ nm).

By taking into account the coupling of dipoles to waveguide modes $\eta_{dp,j}$ absorption $\alpha_{abs,j}$, the altered dipole emission and scattering at the notches, we calculated the expected emission to propagating modes in the glass substrate, depending on the dimensions of the notches (see Figure 10d). The height H is bounded by, and in our case identical to the TiO₂ layer thickness. Again, the base case of $H = 0$ nm is identical to the case of the unperturbed OLED waveguide stack from Table 1a, where 49.2%_{abs} of the emitted power is coupled to the glass substrate. The highest dipole emission to glass of about 76.0%_{abs} is achieved at about $H \approx 220$ nm and $R \approx 120$ nm. While the emission to glass is relatively insensitive to changes in R , we observe multiple local maxima with respect to H , which coincide with strong dipole emission and with heights H (equivalently TiO₂ layer thicknesses) where dipole-to-mode coupling favors TE modes. The latter aspect is not surprising, considering TE modes tend to be less absorbing and are scattered more efficiently, as shown above for the disk-type design.

At RSA maximum density, ≈ 54.7 % of the OLED stack are covered with disks (notches) for the disk-based (notched layer) design. Hence, in both cases, about half of the OLED stack is covered with a TiO₂ layer. Interestingly, both exhibit almost the same optimal or near optimal performance for the same

values of H around 220 to 250 nm. With respect to H both may well be understood as two sides of the same coin, that is, two different models for the same problem, rather than two different designs. However, both models come with distinct drawbacks: The disk model does not include the change in dipole emission (i.e., the Purcell factor), while the notch model implicates that patches of TiO_2 are always large enough for propagating waveguide modes (hence the relative invariance with respect to R).

4. Conclusion

We have revisited the issue of waveguide mode losses in OLEDs and used our own method (based on FEM simulations) to calculate those losses to account for 50.8%_{abs} of the total emitted power, which is in line with the calculation by other methods.^[1] We further identified the competition of absorption and scattering within those modes as the reason of losses, rather than coupling and out-coupling alone. To overcome this issue, we proposed an internal scattering structure based on planarized high refractive index TiO_2 nanodisks to effectively couple out the waveguide modes. For a fabricated sample, we experimentally achieve a 44.2%_{rel} increase in EQE. However, our numerical modeling reveals that only part of this improvement can be attributed to out-coupling of waveguide modes, since power share emitted into the glass substrate only increases from 49.2%_{abs} (with flat interfaces) to 56.2%_{abs} (with internal outcoupling structure). The additional efficiency gain is likely caused by the scattering of substrate modes by the implemented structure. By comparing the calculated absorption lengths for the various waveguide modes with spatial correlations in the internal scattering structure, we find that light extraction from waveguide to radiation modes is likely a two-step process: First occurs the extraction of waveguide to substrate modes, which are subsequently scattered into radiation modes.

Based on our findings, we numerically evaluated a number of further design improvements based on the same concept for the internal scattering structure. The best design increases the power share emitted to glass from 49.2%_{abs} to 79.1%_{abs}. Taking into account all the numerically evaluated approaches to improve the internal outcoupling structure, we can draw more general insights on similar structures and infer a set of basic design rules:

- a) The scattering layer should be in close proximity to the OLED layer stack to ensure strong interaction of waveguide modes with the structure. Note, that for our experimental device, planarization was achieved by a spin-coated polymer layer requiring a minimum thickness (see Experimental section) which leads to a finite proximity. More sophisticated planarization methods, for example, a combination of spin-coating and etching, may help overcome this limitation in a future work.
- b) The thickness, height H should be carefully chosen to maximize dipole emission and to draw power into less absorbing, easy to scatter modes, for example, TE modes are preferable over (plasmonic) TM modes.

- c) The high-index patches should be large enough for propagating modes to form. The shape of the scattering structures seems to be of minor effect, as for instance notches and disks work equally well.

These rules are specific for device configurations where the electrically active OLED stack remains planar, and out-coupling is achieved by a binary variation of refractive index near to it. Furthermore, it is debatable which fraction of the scattering layer should be filled with high-index material. Our modeling thus far simply assumes, that scattering increases linearly with scatterer density. However, for both the disk-based and the notch-based design, we limited our investigation to the maximum RSA fill fraction of 0.547, that is, in both cases, about half of the scattering layer is filled with high-index material. Near the optimum height $H = 220$ nm, both facilitate emission to glass equally well (76.8%_{abs} and 76.0%_{abs}, respectively). If the disk density (notch density) were further increased, the scattering layer would increasingly resemble a closed layer (non-existent layer) of TiO_2 , with likely decreased scattering. This reasoning may lead to the assumption, that about half of the scattering layer should be filled with high-index material for optimal performance, however, more research is required before a solid design rule can be cast from these observations.

Furthermore, if propagation lengths of the waveguide modes are sufficiently long compared to the correlation lengths of the structure, strong correlations (e.g., in the case of periodic patterns) may have a significant impact on the extraction efficiencies (see Section 3.2). A future investigation should therefore cover the combined effects of structure factor, individual disk's response and propagation lengths on extraction efficiencies through theoretical modeling; angle-resolved scatterometry of substrate modes (e.g., via an extraction sphere) may prove useful for experimental confirmation.

On a side note, the stated rules leave plenty of room to optimize such internal structure not only for out-coupling of waveguide modes, but also for substrate-to-air mode coupling. The latter is primarily related to structural correlations (see arrows for Δk_{\parallel} in Figure 7) of the individual scattering elements, and the proposed design rules do not impose any direct restrictions in this respect. Note, however, that spatial correlations in the structure should not be aimed at direct out-coupling of waveguide modes to radiation modes. For correlations to be effective in providing enough parallel component to the wave vector for direct scattering to radiation modes, propagation lengths of waveguide modes need to be sufficiently long. Given that losses are determined by the relation of absorption and scattering, and absorption lengths can only be influenced to a limited degree, trying to optimize for direct coupling to radiation modes would, in most cases, lead to higher losses.

5. Experimental Section

Fabrication of Substrates with Integrated Scattering Layers: Integrating the TiO_2 disk structure into the substrate was achieved by first fabricating the disks on a flat glass surface and subsequent planarization. The detailed disk fabrication process is published in ref. [29], including relevant parameters for the involved processes, and is therefore only summarized briefly here. The fabrication started with a layer stack of 12 nm Al_2O_3 (bottom), 199 nm TiO_2 , and 17 nm Al_2O_3 (top), where all the layers

were deposited by atomic layer deposition (ALD) and all thicknesses were determined by spectroscopic ellipsometry.^[28] Note, that for the relevant wavelength range in this work, the amorphous TiO₂, deposited at 120 °C, was practically non-absorbing (see Figure S1, Supporting Information).^[39] The disk pattern was defined by 406 nm diameter colloidal PMMA particles (microParticles Berlin GmbH, Germany) that adhere to the surface of the Al₂O₃ top layer through opposite charge signs of the two, thereby forming a sparse particle layer throughout the substrate. The particles were heated to 150 °C for 30 min for improved substrate contact and subsequently served as an etch mask to pattern the underlying thin film stack in a two-step reactive ion etching (RIE) process. The excess diameter of the fabricated disks compared to the particle diameter was likely due to the increase in contact area particle-substrate after the heat treatment. The TiO₂ disks were finally planarized by a spin-coated polymer layer (SU-8 negative photoresist, MicroChem) of 450 to 500 nm thickness, which was the minimum possible thickness while at the same time ensuring a planar interface for the subsequent OLED fabrication; thinner layers typically led to corrugated interfaces. The SU-8 planarization layer was baked at a temperature 10 °C higher than the process temperature of the subsequent ITO deposition for 5 min, in order to stabilize the SU-8 and prevent crack formation in the ITO.^[40]

OLED Fabrication: The deposition process of the electrically active layers followed the same protocol and parameters as described in ref. [27], starting with the ITO anode layer of 135 nm thickness on top of the planar polymer layer. The subsequently deposited OLED stack consisted of 5 nm MoO₃, 15 nm m-MTDATA, 20 nm m-MTDATA:Ir(ppy)₃, 20 nm BPhen:Ir(ppy)₃, 40 nm BPhen, 1 nm LiF, and 100 nm aluminum.

OLED Characterization: In order to obtain the EQE, the luminous flux was measured using an integrating sphere and a spectrometer (Instrument Systems CAS140) under nitrogen atmosphere to prevent degradation of the device. For angle resolved emission, the sample was mounted on a rotating stage and the emitted light recorded with a spectrometer (Ocean Optics USB2000+). The sample edges were covered to block substrate mode emission.

Optical characteristics of the planarized nanodisk scattering structure were extracted out of transmittance (*T*) and reflectance (*R*) data, which were measured using a UV-vis spectrometer (Lambda 1050, PerkinElmer Inc.) equipped with a 150 mm integrating sphere. The diffused transmittance of the substrate was performed by letting the direct transmittance escape from the integrating sphere. The haze of the substrate was then derived by taking the ratio of the sole diffused transmitted light to the overall transmitted light.

Numerical: The layer stack constituted a waveguide structure with translation invariance in the lateral direction and thus can be described as a 1D problem along the z-direction:^[41]

$$\nabla \times \mu^{-1} \nabla \times \mathbf{E}_{m,j,1D}(z) - \varepsilon(z) \omega \mathbf{E}_{m,j,1D}(z) = 0 \quad (3)$$

The eigenmodes *j* take the form of plane waves with an effective refractive index *n_{eff,j}* or, equivalently, a propagation constant $\beta = |\boldsymbol{\beta}|$, where $\boldsymbol{\beta}$ is a propagation vector perpendicular to *z*. The electric field is $\mathbf{E}_{m,j,1D}$ and magnetic field is $\mathbf{H}_{m,j,1D}$. Equation (3) was solved by means of the finite element method, which yielded three solutions for which the intensities $|\mathbf{E}|^2$ along *z* are displayed in Figure 1 (right).

An emitter molecule can be described as dipole *i*, of which part of the field $\mathbf{E}_{s,i}$ couples to these guided modes. To calculate the power loss through guided modes, first $\mathbf{E}_{s,i}$ was calculated within the layer stack on a computational domain of height *z_{max}* of cylindrical symmetry by means of the finite element method (Figure 11). The share that couples to a waveguide mode *j* can then be expanded into the respective eigenmode:^[41]

$$\mathbf{E}_{s,i} = \sum_j \mathbf{E}_{m,j}, \mathbf{E}_{s,i} \mathbf{E}_{m,j} \quad (4)$$

The weight of each mode is given by the overlap integral, however, the dipole field can propagate in any direction φ . It is therefore reasonable to calculate the overlap on a small element of the lateral surface with angle increment $\Delta\varphi$ (Figure 11) and surface normal $\mathbf{n}(\varphi)$:

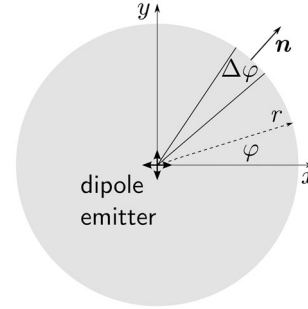


Figure 11. Top view of the cylindrical simulation domain (gray) with centered dipole emitters (one for each spacial orientation, z-direction not shown).

$$S_{i,j}(\varphi) = \mathbf{E}_{m,j}, \mathbf{E}_{s,i} = \frac{1}{2} \int_0^h r \Delta\varphi \mathbf{n}(\varphi) \cdot (\mathbf{E}_{s,i} \times \mathbf{H}_{m,j}(\varphi)) dz \quad (5)$$

$$\text{with } \mathbf{H}_{m,j}(\varphi) = \mathbf{R}_z(\varphi) \mathbf{H}_{m,j,1D} \quad (6)$$

where $\mathbf{R}_z(\varphi)$ is the rotation matrix around the z-axis. The total emitted power of a dipole via the lateral surface *A* is given by

$$P_i = \frac{1}{2} \text{Re} \left\{ \int_A (\mathbf{E}_{s,i} \times \mathbf{H}_{s,i}^*) \cdot d\mathbf{n} \right\} \quad (7)$$

The dipole fields are qualified according to Equations (4) and (5), such that only the share emitted in one particular mode *j* is considered, and the result plugged into Equation (7). After minimizing $\Delta\varphi$ and integration over the entire lateral surface, the coupled power of dipole *i* was obtained to a mode continuum with profile *j*:

$$P_{i,j} = \frac{1}{2\pi} \int_0^{2\pi} |S_{i,j}(\varphi)|^2 d\varphi \quad (8)$$

The emitter molecules Ir(ppy)₃ were approximately randomly oriented and were therefore characterized as dipoles *i* with three possible orientations along *x*, *y*, and *z*-direction.^[42] As basis for any possible dipole orientation, the following calculations were performed for three dipoles aligned in *x*, *y*, and *z*-direction, respectively. The total emitted power per dipole *P_{s,i}* was obtained by integrating the energy flux over a closed surface surrounding the dipole. The average coupling efficiency of all possible dipole orientations to a particular mode is then given by

$$\eta_{dp,j} = \frac{\sum_i P_{i,j}}{\sum_i P_{s,i}} \quad (9)$$

Note, that Equation (8) is valid only for non-absorbing media, in which case the size of the computational domain is irrelevant. However, in particular the aluminum in the real device led to strong absorption losses, that are a central part of the discussion in the main manuscript. Additionally, Equation (3) was solved assuming absorbing aluminum and almost identical mode profiles to the non-absorbing case were observed (see Figure S6, Supporting Information), that is, the real parts $\text{Re}\{n_{\text{eff},j}\}$ of the refractive indices differ by <0.01. Hence, we consider absorbing and non-absorbing waveguide modes sufficiently similar to use the non-absorbing modes for the purpose of calculating the coupling efficiency.

All numerical calculations were performed using the commercially available finite element (FEM) solver JCMsuite. For the 3D simulations, Maxwell's equations were solved on a computational domain with perfectly matched layer boundaries and of cylindrical symmetry, which allowed swift calculation even of 5000 variants of nanodisk dimensions. Radius *R_{CD}* and height *H_{CD}* of the respective computational domain are given in the figure captions.

Supporting Information

Supporting Information is available from the Wiley Online Library or from the author.

Acknowledgements

The authors thank Claudia Stehr and Bodo Fuhrmann for their excellent technical support. Furthermore, P.M.P., R.B.W., and A.N.S. thank JCMwave (Berlin) for providing additional solver licenses. Y.J.D. gratefully acknowledges support from the Max Planck School of Photonics. Y.J.D. and G.G. also acknowledge the Karlsruhe School of Optics & Photonics. The authors thank the Deutsche Forschungsgemeinschaft (DFG) for funding through Program DFG-SPP 1839 "Tailored Disorder," second period (grants WE4051/19-2, project number 278744673, and GO 2615/2-1, project number 410400458).

Open access funding enabled and organized by Projekt DEAL.

Conflict of Interest

The authors declare no conflict of interest.

Data Availability Statement

The data that support the findings of this study are available from the corresponding author upon reasonable request.

Keywords

colloidal lithography, light extraction, Mie resonators, tailored disorder

Received: October 28, 2022

Revised: February 15, 2023

Published online:

- [1] K. Saxena, V. K. Jain, D. S. Mehta, *Opt. Mater.* **2009**, *32*, 221.
- [2] S. Chen, H. S. Kwok, *Opt. Express* **2010**, *18*, 37.
- [3] G. Gomard, J. B. Preinfalk, A. Egel, U. Lemmer, *J. Photonics Energy* **2016**, *6*, 030901.
- [4] J.-J. Kim, J. Lee, S.-P. Yang, H. G. Kim, H.-S. Kweon, S. Yoo, K.-H. Jeong, *Nano Lett.* **2016**, *16*, 2994.
- [5] R. Liu, Z. Ye, J.-M. Park, M. Cai, Y. Chen, K.-M. Ho, R. Shinar, J. Shinar, *Opt. Express* **2011**, *19*, A1272.
- [6] B. W. Lim, M. C. Suh, *Nanoscale* **2014**, *6*, 14446.
- [7] K. Meerholz, D. C. Müller, *Adv. Funct. Mater.* **2001**, *11*, 251.
- [8] J. Frischeisen, B. Scholz, B. Arndt, T. Schmidt, R. Gehlhaar, C. Adachi, W. Brütting, *J. Photonics Energy* **2011**, *1*, 011004.
- [9] S. Nowy, B. C. Krummacker, J. Frischeisen, N. A. Reinke, W. Brütting, *J. Appl. Phys.* **2008**, *104*, 123109.
- [10] T. D. Schmidt, T. Lampe, D. Sylvinson M. R., P. I. Djurovich, M. E. Thompson, W. Brütting, *Phys. Rev. Appl.* **2017**, *8*, 037001.
- [11] J. Song, K.-H. Kim, E. Kim, C.-K. Moon, Y.-H. Kim, J.-J. Kim, S. Yoo, *Nat. Commun.* **2018**, *9*, 3207.
- [12] C. Jeong, Y.-B. Park, L. J. Guo, *Sci. Adv.* **2021**, *7*, eabg0355.
- [13] R. Wang, L.-H. Xu, Y.-Q. Li, L. Zhou, C. Li, Q.-D. Ou, J.-D. Chen, S. Shen, J.-X. Tang, *Adv. Opt. Mater.* **2015**, *3*, 203.
- [14] W. H. Koo, Y. Zhe, F. So, *Adv. Opt. Mater.* **2013**, *1*, 404.
- [15] B. Jiao, Y. Yu, Y. Dai, X. Hou, Z. Wu, *Opt. Express* **2015**, *23*, 4055.
- [16] T. Lan, L. Liu, J. Xie, D. Chen, H. Shen, J. Wang, Y. Chen, H. Cui, W. Shen, K. Cao, S. Chen, *Opt. Express* **2021**, *29*, 7210.
- [17] W. H. Koo, S. M. Jeong, F. Araoka, K. Ishikawa, S. Nishimura, T. Toyooka, H. Takezoe, *Nat. Photonics* **2010**, *4*, 222.
- [18] W. H. Koo, W. Youn, P. Zhu, X.-H. Li, N. Tansu, F. So, *Adv. Funct. Mater.* **2012**, *22*, 3454.
- [19] W. He, X.-H. Dong, J.-G. Zhou, M.-K. Fung, *J. Mater. Chem. C* **2021**, *9*, 6923.
- [20] C.-H. Chang, K.-Y. Chang, Y.-J. Lo, S.-J. Chang, H.-H. Chang, *Org. Electron.* **2012**, *13*, 1073.
- [21] H.-W. Chang, J. Lee, S. Hofmann, Y. Hyun Kim, L. Müller-Meskamp, B. Lüssem, C.-C. Wu, K. Leo, M. C. Gather, *J. Appl. Phys.* **2013**, *113*, 204502.
- [22] J. B. Preinfalk, T. Eiselt, T. Wehlius, V. Rohnacher, T. Hanemann, G. Gomard, U. Lemmer, *ACS Photonics* **2017**, *4*, 928.
- [23] H.-H. Cho, B. Park, H.-J. Kim, J. Shim, S. Jeon, J.-h. Jeong, J.-J. Kim, *Curr. Appl. Phys.* **2010**, *10*, e139.
- [24] H. Cho, E. Kim, J. Moon, C. W. Joo, E. Kim, S. K. Park, J. Lee, B.-G. Yu, J.-I. Lee, S. Yoo, N. S. Cho, *Org. Electron.* **2017**, *46*, 139.
- [25] J.-W. Kim, J.-H. Jang, M.-C. Oh, J.-W. Shin, D.-H. Cho, J.-H. Moon, J.-I. Lee, *Opt. Express* **2014**, *22*, 498.
- [26] J. Choi, S. Kim, C. H. Park, J. H. Kwack, C. H. Park, H. Hwang, H.-S. Im, Y. W. Park, B.-K. Ju, *ACS Appl. Mater. Interfaces* **2018**, *10*, 32373.
- [27] Y. J. Donie, D. Theobald, S. Moghadamzadeh, A. Mertens, I. M. Hossain, U. W. Paetzold, U. Lemmer, G. Gomard, *Adv. Opt. Mater.* **2020**, *9*, 2001610.
- [28] P. M. Piechulla, L. Muehlenbein, R. B. Wehrspohn, S. Nanz, A. Abass, C. Rockstuhl, A. Sprafke, *Adv. Opt. Mater.* **2018**, *6*, 1701272.
- [29] P. M. Piechulla, B. Fuhrmann, E. Slivina, C. Rockstuhl, R. B. Wehrspohn, A. N. Sprafke, *Adv. Opt. Mater.* **2021**, *9*, 2100186.
- [30] S. Torquato, *Phys. Rep.* **2018**, *745*, 1.
- [31] N. Granchi, R. Spalding, M. Lodde, M. Petruzzella, F. W. Otten, A. Fiore, F. Intonti, R. Sapienza, M. Florescu, M. Gurioli, *Adv. Opt. Mater.* **2022**, *10*, 2102565.
- [32] M-MTDATA in ChemBK CAS Database, [https://www.chembk.com/en/chem/4,4',4''-Tris\(N-3-methylphenyl-N-phenylamino\)triphenylamine](https://www.chembk.com/en/chem/4,4',4''-Tris(N-3-methylphenyl-N-phenylamino)triphenylamine) (accessed: October 2022).
- [33] Bphen in ChemBK CAS Database, <https://www.chembk.com/en/chem/Bphen> (accessed: October 2022).
- [34] We here give the absolute share (%_{abs}) of the total emitted power by the emitter molecule (i.e. 100%_{abs}). The index abs is used to distinguish the percentage from a relative increase in comparison to a reference.
- [35] C. F. Bohren, D. R. Huffman, *Absorption and Scattering of Light by Small Particles*, John Wiley & Sons, Inc., New York **2008**.
- [36] microParticles GmbH, Material properties, <https://microparticles.de/eigenschaften.html> (accessed: October 2022).
- [37] J. B. Preinfalk, F. R. Schackmar, T. Lampe, A. Egel, T. D. Schmidt, W. Brütting, G. Gomard, U. Lemmer, *ACS Appl. Mater. Interfaces* **2016**, *8*, 2666.
- [38] S. Torquato, O. U. Uche, F. H. Stillinger, *Phys. Rev. E* **2006**, *74*, 061308.
- [39] J. Aarik, A. Aidla, A.-A. Kiisler, T. Uustare, V. Sammelselg, *Thin Solid Films* **1997**, *305*, 270.
- [40] Kayaku Advanced Materials, Inc., Processing guidelines for SU-8 resist, https://kayakuam.com/wp-content/uploads/2019/09/SU-82000DataSheet2000_5thru2015Ver4.pdf (accessed: February 2023).
- [41] P.-I. Schneider, N. Srocka, S. Rodt, L. Zschiedrich, S. Reitzenstein, S. Burger, *Opt. Express* **2018**, *26*, 8479.
- [42] A. Graf, P. Liehm, C. Murawski, S. Hofmann, K. Leo, M. C. Gather, *J. Mater. Chem. C* **2014**, *2*, 10298.